

Relativistic analysis of nuclear ground state densities at 135 to 200 MeV

M A SUHAIL¹, N NEELOFER² and Z A KHAN³

¹Department of Applied Physics, Z.H. College of Engineering and Technology, Aligarh Muslim University, Aligarh 202 002, India

²Physics Section, Women's College, Aligarh Muslim University, Aligarh 202 002, India

³Department of Physics, Aligarh Muslim University, Aligarh 202 002, India

E-mail: masuhail@lycos.com; nneelofer@lycos.com; zak_atif@yahoo.com

MS received 8 March 2004; revised 26 May 2005; accepted 22 July 2005

Abstract. A relativistic analysis of $p + {}^{40}\text{Ca}$ elastic scattering with different nuclear ground state target densities at 135 to 200 MeV is presented in this paper. It is found that the IGO densities are more consistent in reproducing the data over the energy range considered here. The reproduction of spin-rotation-function data with the simultaneous fitting of differential cross-section and analyzing power, and the appearance of wine-bottle-bottom shaped $\text{Re } U_{\text{eff}}(r)$ in the transition energy region, sensitively depends on the input nuclear ground state densities and are not solely the relativistic characteristic signatures. We also found that the wine-bottle-bottom shaped $\text{Re } U_{\text{eff}}(r)$ is preferred by the spin observables in the transition energy region (i.e. 181 MeV to 200 MeV).

Keyword. Dirac phenomenology.

PACS Nos 24.10.Ht; 25.40.Cm

1. Introduction

It has already been established that the relativistic analyses of proton elastic scattering have an edge over the conventional Schrödinger equation-based non-relativistic approaches [1,2]. The previous fits to the experimental data for elastic proton scattering at intermediate energy region suggested the need of a real effective optical potential that deviates from a Fermi-distribution-like shape [3,4]. Dirac equation optical model calculations [5] lead to the real effective optical potentials with wine-bottle-bottom shape associated to an intrinsic relativistic effect [1,5]. G -matrix is also able to obtain such behaviour [6].

Here, we have adopted the phenomenological relativistic approach in which a relativistic Dirac equation is simplified, using standard rigorous mathematical techniques, to an equivalent Schrödinger equation containing complex central ($U_{\text{eff}}(r)$)

and spin-orbit ($U_{\text{so}}(r)$) optical potentials [1,5]. These $U_{\text{eff}}(r)$ and $U_{\text{so}}(r)$ are further written in terms of the complex Lorentz scalar ($U_s(r)$) and the time-like component of Lorentz vector ($U_0(r)$) potentials. These potentials are Lorentz invariant and hence the equivalent Schrödinger equation is purely relativistic in its character. The real parts of $U_s(r)$ and $U_0(r)$ potentials are obtained through the folding procedure, where the matter densities of the target nucleus and the parametrized effective NN interactions are used as an input, as is described in detail in §2. The respective imaginary parts of these potentials are directly taken from refs [5,7]. The imaginary parts of $U_s(r)$ and $U_0(r)$ potentials are not uniquely determined. So, the imaginary part of $U_{\text{eff}}(r)$, which is nothing but a combination of the imaginary parts of $U_s(r)$ and $U_0(r)$ potentials, is naturally not uniquely defined. Hence it may lead to ambiguities in the results. But, the role of imaginary $U_{\text{eff}}(r)$ in the fitting of elastic scattering observables at low and intermediate energies is not very significant and hence one can still go ahead with such potentials.

The strengths of real and imaginary parts of complex $U_s(r)$ and $U_0(r)$ potentials are multiplied with their respective normalization constants λ_s^r , λ_s^i , λ_v^r and λ_v^i (collectively called as λ 's). These complex $U_s(r)$ and $U_0(r)$ potentials are then renormalized varying λ 's through chi-square minimization to fit the experimental data of elastic scattering observables. The values of λ 's, if close to unity, imply that the calculated potentials are more realistic.

It is well-known that both non-relativistic and relativistic calculations have an uncertainty associated with the structure of the underlying target nucleus [5,8,9] and thus it is expected that different target nuclear densities predict elastic scattering observables differently. So, we analyze the $p + {}^{40}\text{Ca}$ elastic scattering phenomenologically for different nuclear ground state densities using relativistic Dirac equation at 135 MeV, 160 MeV, 181 MeV and 200 MeV. The source of data used here is given in refs [7,10,11]. The results are found to be very sensitive to the shapes of real $U_s(r)$ and $U_0(r)$ potentials. These potentials follow, more or less, the shape of the nuclear ground state densities in the folding model. So, the effect of different nuclear density distributions is quite conspicuous in the relativistic approach. Hence, we have analyzed five different nuclear ground state densities for the target ${}^{40}\text{Ca}$. These densities are given by L Ray (LRAY) [12–15], Chaumeaux *et al* (CHMX) [16], Igo *et al* (IGO) [17], Negele (NEG) [18] and the folded Negele densities (FNEG) [5]. We find that the wine-bottle-bottom shaped $\text{Re } U_{\text{eff}}$ in the transition energy region and the good prediction of spin-rotation-function data, obtained from the simultaneous fitting of differential cross-section and analyzing power, is not the relativistic characteristic signature [2,5], rather they sensitively depend on the nuclear ground state densities. It is seen that a little variation in the radial distribution of $\text{Re } U_{\text{eff}}$ in the surface region may cause a drastic change in the fitting of scattering observables. Further, we find that in the transition energy region (i.e. 181–200 MeV) the wine-bottle-bottom shaped $\text{Re } U_{\text{eff}}$ reproduces the spin observables quite satisfactorily. The results obtained using IGO density [17] are more consistent throughout the energy range considered here.

Section 2 contains a brief mathematical formalism of relativistic Dirac equation and the evaluation of $\text{Re } U_s(r)$ and $\text{Re } U_0(r)$ potentials. Results and discussion are given in §3 and the conclusion in §4.

2. Formalism

The Dirac equation in terms of the rotationally symmetric complex Lorentz scalar, $U_s(r)$, and four-vector, $\gamma^\mu U_{v,\mu}(\vec{r}) = \gamma^0 U_0(r) - \vec{\gamma} \cdot \vec{U}_v^r(r)$, potentials can be written as

$$\{\vec{\alpha} \cdot \vec{p} + \beta[m + U_s] - [E - U_0 - V_c] - \beta\vec{\gamma} \cdot \hat{r}U_v^r\}\psi(\vec{r}) = 0, \quad (1)$$

where $V_c(r)$ is the Coulomb potential, m is the nucleon mass and E is the nucleon total energy in center-of-mass (c.m.) system. The contribution of tensor potential is found to be very insignificant and hence we have not considered it in our calculations. In terms of the upper and lower components of $\psi(\vec{r})$, eq. (1) may be written as

$$\left\{ \begin{pmatrix} 0 & \vec{\sigma} \cdot \vec{p} \\ \vec{\sigma} \cdot \vec{p} & 0 \end{pmatrix} + \begin{pmatrix} m + U_s & 0 \\ 0 & m + U_s \end{pmatrix} - \begin{pmatrix} E - U_0 - V_c & 0 \\ 0 & E - U_0 - V_c \end{pmatrix} - \begin{pmatrix} 0 & \vec{\sigma} \cdot \hat{r} \\ \vec{\sigma} \cdot \hat{r} & 0 \end{pmatrix} U_v^r \right\} \begin{bmatrix} \psi_U(\vec{r}) \\ \psi_L(\vec{r}) \end{bmatrix} = 0. \quad (2)$$

Equation (2) can further be simplified as

$$\vec{\sigma} \cdot \vec{p}\psi_L + (m + U_s)\psi_U - (E - U_0 - V_c)\psi_U - (\vec{\sigma} \cdot \hat{r})U_v^r\psi_L = 0, \quad (3)$$

$$\vec{\sigma} \cdot \vec{p}\psi_U - (m + U_s)\psi_L - (E - U_0 - V_c)\psi_L - (\vec{\sigma} \cdot \hat{r})U_v^r\psi_U = 0. \quad (4)$$

Solving eq. (4) for the lower component in terms of upper component $\psi_U(\vec{r})$, gives

$$\psi_L(\vec{r}) = \frac{1}{(E + m)A(r)} [\vec{\sigma} \cdot \vec{p} - (\vec{\sigma} \cdot \hat{r})U_v^r] \psi_U(\vec{r}) \quad (5)$$

where

$$A(r) = \frac{(m + U_s + E - U_0 - V_c)}{(E + m)}.$$

Substituting eq. (5) in eq. (3) and solving for the upper component $\psi_U(\vec{r})$, gives

$$[(E - U_0 - V_c)^2 - (m + U_s)^2 - Q(r)]\psi_U(\vec{r}) = 0, \quad (6)$$

where

$$Q(r) = A(r) [\vec{\sigma} \cdot \vec{p} - (\vec{\sigma} \cdot \hat{r})U_v^r] \frac{1}{A(r)} \times [\vec{\sigma} \cdot \vec{p} - (\vec{\sigma} \cdot \hat{r})U_v^r]. \quad (7)$$

Carrying out the required algebra, eq. (6) can further be reduced to the following equation (see ref. [1]):

$$\left\{ \nabla^2 + (E - U_0 - V_c)^2 - (m + U_s)^2 - U_v^{r^2} + \left[\frac{1}{rA} \frac{\partial A}{\partial r} \right] (\vec{\sigma} \cdot \vec{L}) \right. \\ \left. - \frac{2}{r} (iU_v^r) + \frac{1}{A} \frac{\partial A}{\partial r} (iU_v^r) + \frac{1}{r} (\vec{r} \cdot \vec{p}) U_v^r \right. \\ \left. - \left[i \frac{1}{rA} \frac{\partial A}{\partial r} - 2 \frac{U_v^r}{r} \right] (\vec{r} \cdot \vec{p}) \right\} \psi_U(\vec{r}) = 0. \quad (8)$$

To remove the first derivative terms, let

$$\psi_U(\vec{r}) = K(r)\phi(\vec{r}), \quad (9)$$

with $K(r) \rightarrow 1$ as $r \rightarrow \infty$. Direct substitution of (9) into (8) gives

$$\frac{\partial}{\partial r} K(r) = \frac{1}{2} \left[\frac{1}{A} \frac{\partial A}{\partial r} - 2iU_v^r \right] K(r), \quad (10)$$

or

$$K(r) = A^{1/2} \exp \int iU_v^r(r) dr. \quad (11)$$

Using eq. (10), we may write the Schrödinger equivalent equation as

$$\left\{ \nabla^2 + (E - U_0 - V_c)^2 - (m + U_s)^2 - \frac{3}{4} \frac{1}{A^2} \left(\frac{\partial A}{\partial r} \right)^2 \right. \\ \left. + \frac{1}{2r^2 A} \frac{\partial}{\partial r} \left(r^2 \frac{\partial A}{\partial r} \right) + \left[\frac{1}{rA} \frac{\partial A}{\partial r} \right] (\vec{\sigma} \cdot \vec{L}) \right\} \phi(\vec{r}) = 0. \quad (12)$$

Notice that the three-vector part of the vector potential does not appear in (12). Neglecting the Darwin term, one may define Schrödinger equivalent complex central and spin-orbit potentials as

$$U_{\text{eff}} = \frac{1}{2E} \left[2EU_0 + 2mU_s - U_0^2 + U_s^2 - 2V_c U_0 \right. \\ \left. + \left(-\frac{1}{2r^2 A} \frac{\partial}{\partial r} \left(r^2 \frac{\partial A}{\partial r} \right) + \frac{3}{4A^2} \left(\frac{\partial A}{\partial r} \right)^2 \right) \right], \quad (13)$$

and

$$U_{\text{so}} = \frac{1}{2E} \left[-\frac{1}{rA} \frac{\partial A}{\partial r} \right]. \quad (14)$$

The Schrödinger equivalent equation in terms of U_{eff} and U_{so} is given as

$$[p^2 + 2E(U_{\text{eff}} + U_{\text{so}})]\phi(\vec{r}) = [(E - V_c)^2 - m^2]\phi(\vec{r}). \quad (15)$$

Now, this equation can be solved for $\phi(\vec{r})$ if U_{eff} and U_{so} are substituted into it. These potentials can be evaluated from eqs (13) and (14) provided $U_s(r)$ and $U_0(r)$ are known. The $U_s(r)$ and $U_0(r)$ potentials may be written as

$$U_j(r) = V_j f_j(r) + iW_j g_j(r) \equiv V_j'(r) + iW_j'(r), \quad (16)$$

with the proviso that $j = s$ for the scalar and $j = 0$ for the vector quantities. The imaginary potentials in eq. (16) have directly been taken from refs [5,7]. The real parts are numerically evaluated as

$$V_j' = \int dr' v_j(|r - r'|) \tilde{\rho}_j(r'), \quad (17)$$

where v_j are the effective NN scalar and vector interactions and $\tilde{\rho}_j(r')$ are the effective scalar and vector densities [5]. The NN effective interaction shows weak energy dependence at low and intermediate energies. This allows us to use the same v_j , evaluated at 181 MeV, at all the energies considered here, i.e. from 135 MeV to 200 MeV. The empirical LRAY, CHMX, IGO and the microscopic FNEG densities used here are the effective baryonic densities (i.e. $\tilde{\rho}_0(r')$) which incorporate the finite size effect of the projectile and the target nucleon, whereas, the NEG density is the microscopic point-like nuclear matter density with Fermi distribution-like parametrization. The NEG and FNEG densities have been used to see the effect of finite size correction at the energies considered here. The effective scalar density (i.e. $\tilde{\rho}_s(r')$) which is empirically undetermined, is approximated as [5]

$$\tilde{\rho}_s(r) = \left[\frac{\rho_s}{\rho_0} \right]_{\text{vol}} \tilde{\rho}_0(r), \quad (18)$$

where

$$0.91 \leq \left[\frac{\rho_s}{\rho_0} \right]_{\text{vol}} \leq 0.98. \quad (19)$$

So, knowing the U_{eff} and U_{so} potentials, the Schrödinger equivalent equation, eq. (15), can now be solved for wave function $\phi(\vec{r})$. Once $\phi(\vec{r})$ is obtained, the scattering amplitude $f(\theta)$ can be easily calculated. This can be written in terms of the complex central and spin-orbit parts as

$$f(\theta) = A(\theta) + B(\theta) \vec{\sigma} \cdot \hat{n}. \quad (20)$$

Now, the scattering observables (i.e. the differential cross-section, polarization or analyzing power and spin-rotation-function) are given as

$$\frac{d\sigma}{d\Omega} = |A|^2 + |B|^2, \quad (21)$$

$$\vec{P} = \frac{2\text{Re} AB^*}{|A|^2 + |B|^2} \vec{n},$$

and

$$Q = \frac{2\text{Im} AB^*}{|A|^2 + |B|^2}. \quad (22)$$

Here, we have not considered the lower component. Indeed for the momentum transfers involved in reactions studied in this paper, this component is quite small [19,20].

These elastic scattering observables have been evaluated using relativistic optical model computer code.

3. Results and discussion

3.1 Analysis of scattering observables

The results obtained for differential cross-section (σ_s) and analyzing power (A_y) (wherever data are available with us) with NEG densities at 135 and 160 MeV and with IGO densities at 160 MeV for the p+ ^{40}Ca elastic scattering give fairly good agreement with the experimental data as is obvious from the total chi-square per degree of freedom (χ^2/DF) in table 1 (see also figures 1 and 2a). The total χ^2/DF at 135 MeV obtained with IGO, LRAY, CHMX and FNEG densities are not satisfactory although these densities incorporate finite size correction

Table 1. The values of normalization constants (λ_s^r , λ_s^i , λ_v^r and λ_v^i) and the χ^2 obtained from the simultaneous fitting of the scattering observables for p + ^{40}Ca elastic scattering at 135–200 MeV, where, ‘200 without SRF’ indicates that spin-rotation-function is not included in the fitting, while ‘200 with SRF’ indicates that it is included.

Energy (MeV)	Density used	λ_v^r	λ_v^i	λ_s^r	λ_s^i	$\chi^2\sigma_s$	χ^2A_y	χ^2Q	χ^2/DF
135	IGO	0.65	1.86	0.68	2.03	49.87	–	–	49.87
	LRAY	0.72	1.12	0.76	1.14	55.26	–	–	60.93
	CHMX	0.71	1.10	0.75	1.11	63.16	–	–	69.64
	FNEG	0.74	0.56	0.79	0.48	73.36	–	–	80.89
	NEG	0.68	2.17	0.71	2.37	22.19	–	–	24.47
160	IGO	0.62	1.90	0.67	2.11	15.98	9.35	–	14.18
	LRAY	0.72	1.24	0.77	1.28	27.20	3.75	–	22.36
	CHMX	0.70	1.16	0.75	1.20	28.66	6.81	–	24.34
	FNEG	0.74	0.50	0.80	0.40	35.26	21.25	–	33.75
	NEG	0.63	2.28	0.68	2.54	17.33	8.94	–	16.15
181	IGO	0.62	1.38	0.67	1.47	31.66	23.17	–	29.39
	LRAY	0.77	1.21	0.82	1.22	33.42	9.95	–	23.52
	CHMX	0.77	1.22	0.82	1.25	34.85	9.40	–	24.02
	FNEG	0.86	1.12	0.92	1.10	54.83	10.22	–	35.43
	NEG	0.63	1.17	0.68	1.17	59.41	15.12	–	40.48
200 without SRF	IGO	0.69	1.03	0.73	1.01	30.94	19.27	38.07	27.05
	LRAY	0.85	1.25	0.89	1.22	31.45	39.34	123.45	49.70
	CHMX	0.83	1.34	0.87	1.35	23.36	44.33	137.67	50.97
	FNEG	0.94	1.26	0.97	1.24	26.50	55.71	325.13	87.56
	NEG	0.70	1.03	0.74	0.97	42.75	17.84	51.92	33.47
200 with SRF	IGO	0.68	0.83	0.73	0.77	33.12	17.80	17.65	26.21
	LRAY	0.78	1.06	0.83	1.03	47.49	33.39	51.64	44.47
	CHMX	0.77	1.02	0.82	0.99	46.58	32.92	38.60	41.63
	FNEG	0.83	1.05	0.88	1.02	66.79	34.48	65.07	55.54
	NEG	0.69	0.86	0.74	0.77	46.64	15.76	30.08	32.35

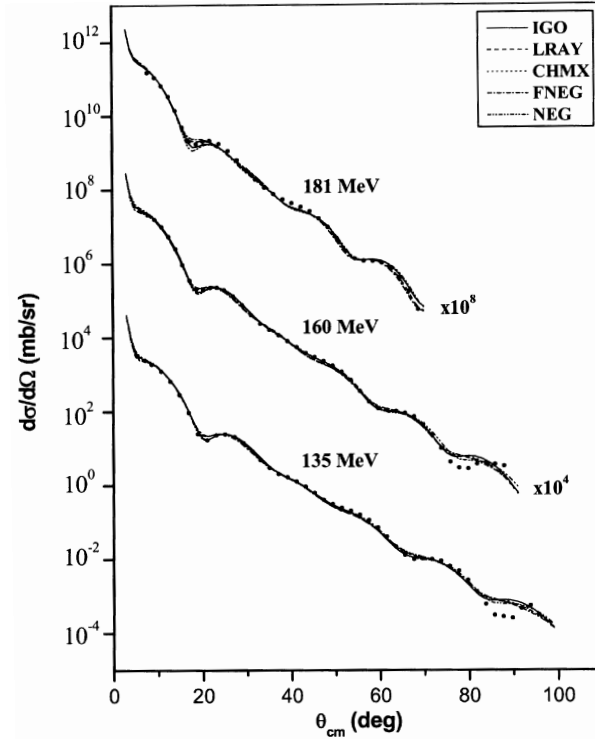


Figure 1. Comparison of the elastic scattering $p + {}^{40}\text{Ca}$ differential cross-section (σ_s) with experimental data [7,10,11] at 135, 160 and 181 MeV, calculated with different target nucleon densities considered here.

(see table 1). It simply implies that the finite size correction does not play a significant role at this energy, whereas, at 160 and 181 MeV the LRAY and CHMX densities predict the analyzing power data noticeably well (see χ^2 of the analyzing power (A_y) in table 1 and also figure 2). The FNEG densities give good chi-square of analyzing power (χ^2 of A_y) at 181 MeV. But, overall, at this energy, LRAY, CHMX, and IGO densities are better as far as total chi-square per degree of freedom (χ^2/DF) is concerned (see table 1, figure 1 at 181 MeV and figure 2b).

The situation at 200 MeV is very different. It implies from the values of χ^2 of σ_s , A_y and spin-rotation-function (Q) that the scattering observables, such as differential cross-section, analyzing power and spin-rotation-function, obtained with IGO densities, follow the experimental data quite accurately (see ‘200 without SRF’ in table 1 and figure 3 ‘without SRF’, figures 4a and 4c). In particular, the good reproduction of spin-rotation-function is noticeable even when it is not included in the fitting along with the differential cross-section and analyzing power data, while, it is not so in the case of other densities considered here (see χ^2 of Q in table 1 for ‘200 without SRF’ and figure 4c). The spin observables, A_y and Q , calculated with LRAY, CHMX, NEG, and FNEG densities noticeably improve their agreement with the experimental data at 200 MeV if the spin-rotation-function is also included in

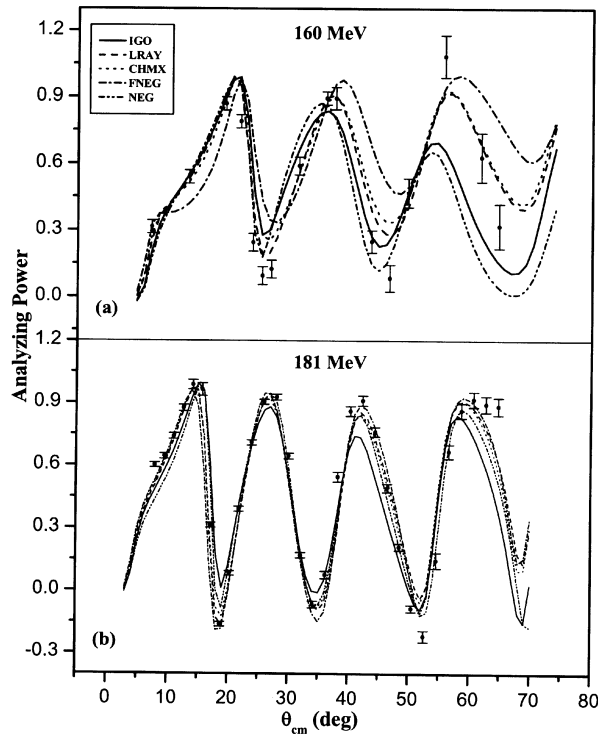


Figure 2. Comparison of elastic scattering $p + {}^{40}\text{Ca}$ analyzing power (A_y) with experimental data [7,10,11] at 160 and 181 MeV, calculated with different target nuclear densities considered here.

the fitting (see ‘200 with SRF’ in table 1 and figures 4b and 4d). Of course, this improvement occurs at the cost of the fitting of the differential cross-section (figure 3 ‘with SRF’) but the scattering observables calculated with IGO densities remain almost unaltered (see ‘200 with SRF’ in table 1 and figures 4b and 4d). So, we conclude that the fairly good prediction of spin-rotation-function data from the simultaneous fitting of the differential cross-section and analyzing power is not solely a relativistic characteristic signature. But, it also sensitively depends on the nuclear ground state densities. The adequate reproduction of the spin observables at 200 MeV with IGO densities is further important because this region is the transition energy region where, strong cancellation of scalar and vector potentials take place and $\text{Re } U_{\text{eff}}$ changes its shape predominantly from attractive to repulsive [21,22]. Hence, this region is always difficult for reproducing the experimental data [23].

In our analysis we found that the IGO densities are more realistic when compared to LRAY, CHMX, NEG and FNEG densities (table 1). The nuclear ground state densities used here may now be placed in the order of merit as follows (see table 1): IGO, LRAY, CHMX, NEG and FNEG.

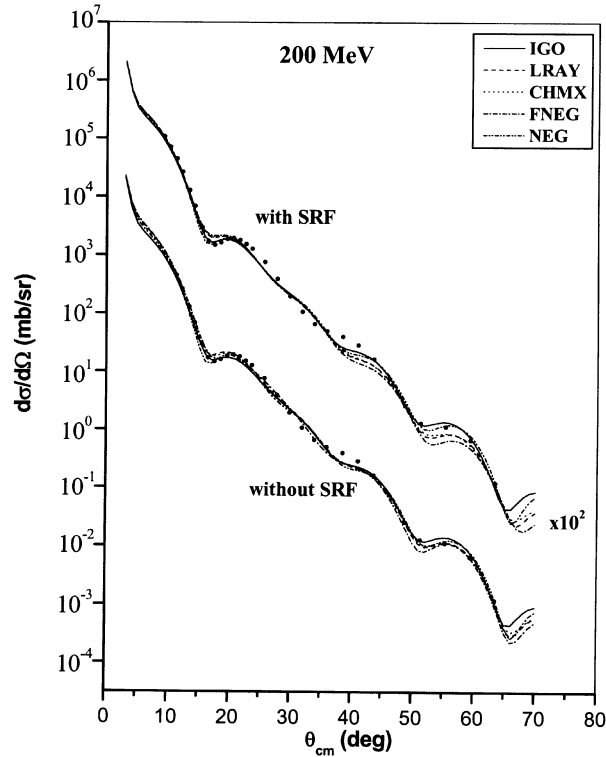


Figure 3. Same as figure 1, at 200 MeV, with and without SRF included in the fitting.

3.2 Analysis of $\text{Re } U_{\text{eff}}$

The radial distribution of the ground state nuclear densities is shown in figure 5a. The minute differences in their surface region are quite important. It would be discussed in detail later. Figure 5b depicts the plots of $\text{Re } U_s(r)$ and $\text{Re } U_0(r)$ potentials obtained through the folding model with different nuclear ground state densities used in this analysis. The depths of these potentials corresponding to different densities are given in table 2. The imaginary $U_s(r)$ and $U_0(r)$ potentials calculated at 181 MeV in [5] are used here at energies 135, 160 and 181 MeV, whereas, at 200 MeV the required imaginary potentials are directly taken from [7]. The depths of these potentials are given in the caption of table 2. When these imaginary potentials are fed into eqs (13) and (14), they give rise to the imaginary parts of $U_{\text{eff}}(r)$ and $U_{\text{so}}(r)$ optical potentials, i.e. $\text{Im } U_{\text{eff}}(r)$ and $\text{Im } U_{\text{so}}(r)$. The radial variations of $\text{Re } U_{\text{eff}}$ obtained for $p + {}^{40}\text{Ca}$ elastic scattering at 135 to 200 MeV for all the densities considered here are shown in figures 6 and 7.

The $\text{Re } U_{\text{eff}}$ at the energies considered here, for all densities, show a vast variation in the interior region (shown in figures 6 and 7) although the corresponding chi-squares are close to each other (table 1). On the other hand, the $\text{Re } U_{\text{eff}}$ lying close

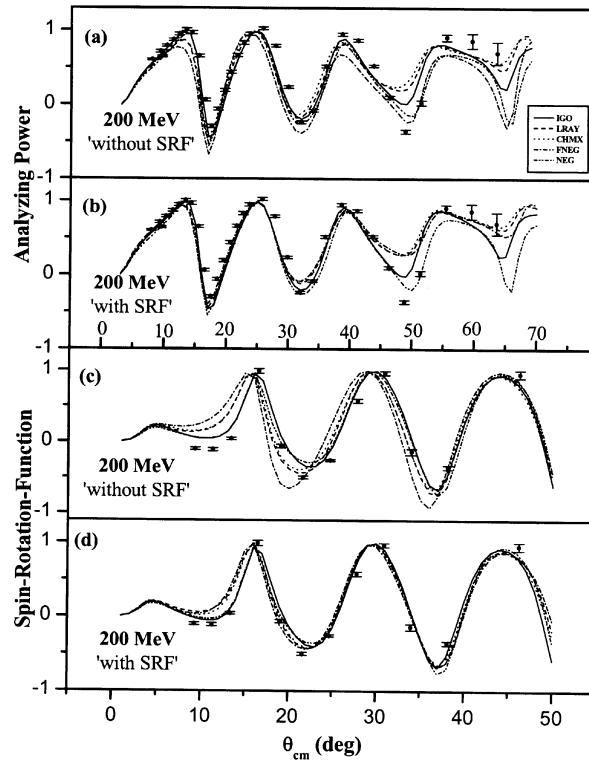


Figure 4. Analyzing power and spin-rotation-function [7,10,11] at 200 MeV, calculated with different target nuclear densities considered here, with and without SRF included in the fitting.

Table 2. These are the depths of $Re U_s$ and $Re U_0$ potentials evaluated at 181 MeV [5] and used at all energies considered here, i.e. 135 MeV to 200 MeV. The respective imaginary potentials are taken from ref. [5]. Their depths are $Im U_s = 108.02$ MeV and $Im U_0 = -105.93$ MeV. These potentials are used at 135 MeV, 160 MeV and 181 MeV, whereas, the imaginary potentials at 200 MeV are directly taken from ref. [7] and their depths are $Im U_s = 87.81$ MeV and $Im U_0 = -81.68$ MeV.

Potential depths	Densities used				
	IGO	LRAY	CHMX	FNEG	NEG
$Re U_s$	-499.56	-501.39	-490.51	-472.71	-481.28
$Re U_0$	406.76	409.05	400.05	385.20	390.94

to each other in the interior region, such as shown by the graphs corresponding to LRAY, CHMX and FNEG densities (figures 6 and 7), show a vast difference in their chi-squares (table 1). This clearly indicates that the interior region of $Re U_{eff}$ does not play a meaningful role in the $p + {}^{40}\text{Ca}$ elastic scattering at the

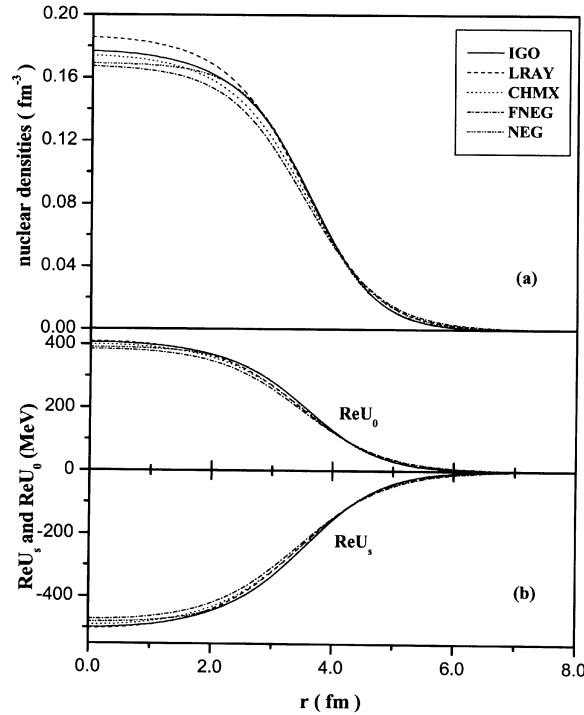


Figure 5. Radial distribution of ground state nuclear matter densities (IGO [17], LRAY [12–15], CHMX [16], NEG [18], and FNEG [5]) for ^{40}Ca and the real parts of $U_s(r)$ and $U_0(r)$ potentials obtained through the folding model procedure, using these densities.

energies considered here. It further strengthens the well-known fact that the elastic scattering observables, at intermediate energies, are surface peaked. So, it is the surface part of $\text{Re}U_{\text{eff}}$, which mainly contributes in the reproduction of the elastic scattering data. This surface region of $\text{Re}U_{\text{eff}}$ sensitively depends on the shapes of $\text{Re}U_s$ and $\text{Re}U_0$ potentials. In the folding model, the input ingredient nuclear ground state densities govern these shapes. Hence, even a minute difference in the surface region in the radial distribution of the densities is quite important. Therefore, we conclude that the relativistic analysis of $p + ^{40}\text{Ca}$ elastic scattering with different nuclear ground state densities of the target, will always be more revealing regarding the role and the nature of the densities.

At 135 MeV, the $\text{Re}U_{\text{eff}}$ corresponding to all densities are Fermi-shaped (figure 6a). The difference in $\text{Re}U_{\text{eff}}$ calculated with IGO and NEG densities in the surface region is very minute (figure 6a). However, it is still quite crucial and leads to the noticeable difference in the chi-squares (table 1). On the other hand, at 160 MeV the $\text{Re}U_{\text{eff}}$ corresponding to IGO and NEG densities almost overlap (figure 6b) and hence their chi-squares are quite close to each other (table 1). Therefore, it is quite evident from here that the scattering observables sensitively depend on the surface region of the $\text{Re}U_{\text{eff}}$, which is mainly governed by the input nuclear ground state densities.

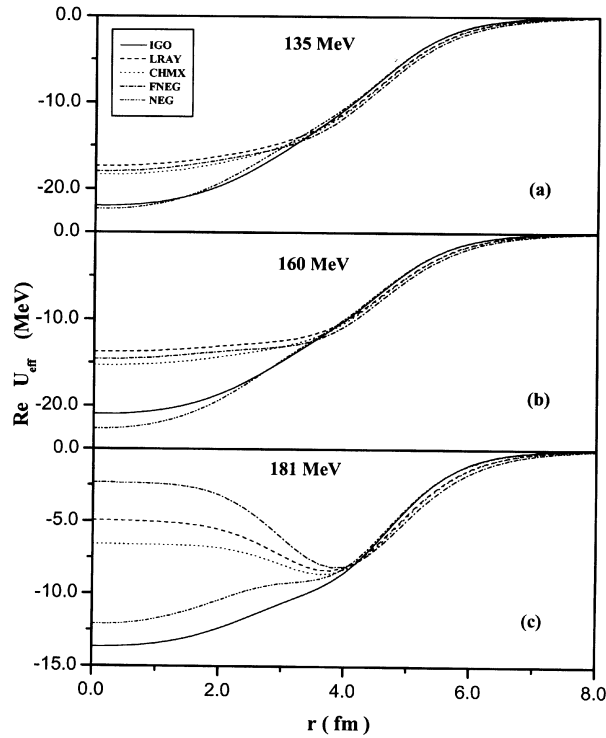


Figure 6. Real part of the Schrödinger equivalent potentials (i.e. $\text{Re } U_{\text{eff}}$) calculated with the densities of figure 5, for $p + {}^{40}\text{Ca}$ elastic scattering at 135, 160 and 181 MeV.

The $\text{Re } U_{\text{eff}}$ calculated at 181 MeV with LRAY, CHMX and FNEG densities take a wine-bottle-bottom shape (figure 6c). The analyzing power calculated with such $\text{Re } U_{\text{eff}}$ give a good agreement with the experimental data (table 1, figure 2b). The $\text{Re } U_{\text{eff}}$ calculated with NEG densities has a shallow wine-bottle-bottom shape at 181 MeV (figure 6c) but still give satisfactory χ^2 for A_y (table 1). However, the $\text{Re } U_{\text{eff}}$ obtained at this energy using IGO densities does not have a wine-bottle-bottom shape at all (figure 6c) and so, does not reproduce the analyzing power data well (see χ^2 for A_y in table 1 and figure 2b). While, at 200 MeV, it is only the IGO and NEG densities, which lead to the wine-bottle-bottom shaped $\text{Re } U_{\text{eff}}$ (figure 7a) and hence reproduces the spin observables remarkably well (see ‘200 without SRF’ in table 1 and figures 4a and 4c). Such $\text{Re } U_{\text{eff}}$ predicts the spin-rotation-function adequately well even if it is not included in the fitting (see ‘200 without SRF’ in table 1 and figure 4c). When the spin-rotation-function data are also included in the fitting, along with the differential cross-section and analyzing power, the obtained $\text{Re } U_{\text{eff}}$ for all the densities tends to acquire a more pronounced wine-bottle-bottom shape (figure 7b) and hence improve the fitting of the spin observables (see χ^2 of A_y and Q in table 1 for ‘200 with SRF’ and figures 4b and 4d). This clearly implies that the emergence of the wine-bottle-bottom shape of the $\text{Re } U_{\text{eff}}$ in the transition energy region (181–200 MeV) is not an intrinsic relativistic characteristic signature,

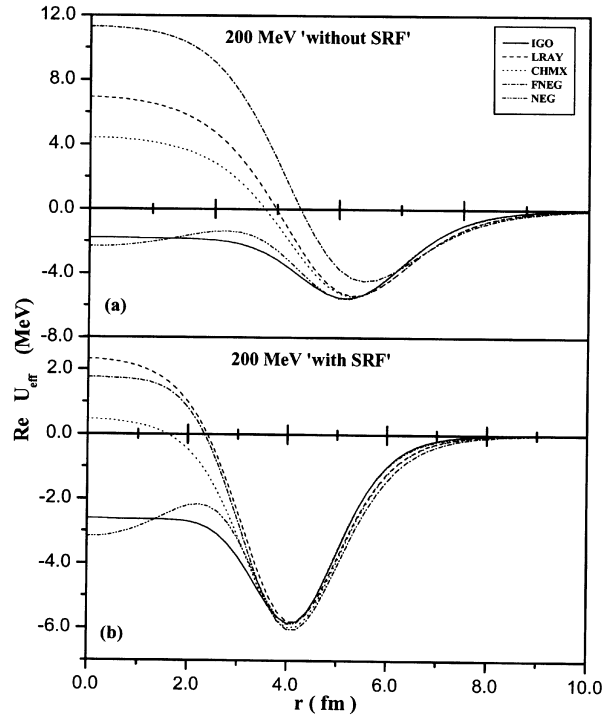


Figure 7. Same as figure 6, at 200 MeV, with and without SRF included in the fitting.

rather it also, sensitively, depends on nuclear ground state densities. Further, the good reproduction of spin-rotation-function, calculated from the fitting of differential cross-section and analyzing power, is an intrinsic characteristic signature of the wine-bottle-bottom shaped $\text{Re } U_{\text{eff}}$ which is prominently governed by the input nuclear ground state densities and not solely by the relativistic formalism itself. Such potentials are preferred by the spin observables in the transition energy region.

4. Conclusion

We conclude that the relativistic analysis of the nuclear ground state densities is a better choice. IGO densities are found to be more realistic, when compared to other densities considered here. We further conclude that the prediction of spin-rotation-function from the simultaneous fitting of differential cross-section and analyzing power data and the wine-bottle-bottom shaped $\text{Re } U_{\text{eff}}$ in the transition energy region are not solely the relativistic characteristic signatures, rather the above situation also depends sensitively on the input nuclear ground state densities. The smoothly varying, throughout attractive, wine-bottle-bottom shaped $\text{Re } U_{\text{eff}}$, as is obtained with IGO densities at 200 MeV, reproduces the spin observable more accurately. In particular, the spin-rotation-function is well reproduced by such

$\text{Re}U_{\text{eff}}$ even if it is not included in the fitting. We have also seen that the role of finite size correction of the nucleon, at the energies considered here, in particular at 135 MeV, is not very significant. The fitting of the scattering observables at all energies and for all densities considered here sensitively depends on the surface part of $\text{Re}U_{\text{eff}}$. A little variation in the surface region of $\text{Re}U_{\text{eff}}$ may significantly change the final results.

Acknowledgement

We are extremely thankful for the referee's valuable comments and suggestions which helped us to improve our manuscript in several ways.

References

- [1] B C Clark, S Hama and R L Mercer, in: The interactions between medium energy nuclei – 1982 edited by H O Meyer, *AIP Conf. Proc. No. 97* (AIP, New York, 1983) p. 260
- [2] B C Clark, S Hama, R L Mercer, L Ray and B D Serot, *Phys. Rev. Lett.* **21**, 1644 (1983)
- [3] L R B Elton, *Nucl. Phys.* **89**, 69 (1966)
- [4] H O Meyer, P Schwandt, G L Moake and P P Singh, *Phys. Rev.* **C23**, 616 (1981)
- [5] L G Arnold, B C Clark, R L Mercer and P Schwandt, *Phys. Rev.* **C23**, 1949 (1981)
- [6] L Rikus, K Nakano and H V Von Geramb, *Nucl. Phys.* **A414**, 413 (1984)
- [7] D A Hutcheon *et al*, *Nucl. Phys.* **A483**, 429 (1988)
- [8] A Picklesimer, P C Tandy, R M Thaler and D H Wolfe, *Phys. Rev.* **C30**, 186 (1984)
- [9] R Crespo, R C Johnson and J A Tostevin, *Phys. Rev.* **C50**, 2995 (1994)
- [10] P Schwandt, H O Meyer, W W Jacobs, A D Bacher, S E Vigdor, M D Kaitchuck and T D Donoghue, *Phys. Rev.* **C26**, 55 (1982)
- [11] D A Hutcheon *et al*, in *Polarization phenomenon in nuclear physics* (AIP Conf., 1981) vol. 69, p. 454
- [12] C W Jager De, H D Vries and C D Vries, *Nucl. Data Tables* **14**, 479 (1974)
- [13] G W Hoffmann *et al*, *Phys. Rev.* **C21**, 1488 (1980)
- [14] L Ray, G W Hoffmann, G S Blanpied, W R Coker and R P Liljestrang, *Phys. Rev.* **C21**, 1756 (1978)
- [15] L Ray, *Phys. Rev.* **C19**, 1855 (1979)
- [16] A Chaumeaux, V Layly and R Schaeffer, *Ann. Phys.* **116**, 247 (1978)
- [17] G Igo *et al*, *Phys. Lett.* **B81**, 151 (1979)
- [18] J W Negele, *Phys. Rev.* **C1**, 1260 (1970)
- [19] E D Cooper and H S Sherif, *Phys. Rev.* **C25**, 3024 (1982)
- [20] R Shyam, W Cassing and U Mosel, *Nucl. Phys.* **A586**, 557 (1995)
- [21] M Jaminin, C Mahaux and P Rochus, *Phys. Rev.* **C22**, 2027 (1980)
- [22] P Schwandt, in: The interaction between medium energy nucleons in nuclei – 1982 edited by H O Meyer, *AIP Conf. Proc. No. 97* (AIP, New York, 1983) p. 89
- [23] W Haider, J R Rook and A M Kobos, *Nucl. Phys.* **A480**, 20 (1988)